Monthly Notices
of the
ROYAL ASTRONOMICAL SOCIETY

MNRAS **476,** 235–245 (2018)
Advance Access publication 2018 January 16

doi:10.1093/mnras/sty129

The magnetic field in the central parsec of the Galaxy

P. F. Roche,[1⋆] E. Lopez-Rodriguez,[2,3] C. M. Telesco,[4] R. Schödel[5] and C. Packham[3,6]

[1]*Astrophysics, Department of Physics, University of Oxford, DWB, Keble Road, Oxford OX1 3RH, UK*
[2]*SOFIA Science Center, NASA AmesResearch Center, Moffett Field, CA 94035, USA*
[3]*Department of Physics and Astronomy, University of Texas at San Antonio,1 UTSA Circle, San Antonio, TX 78249, USA*
[4]*Department of Astronomy, University of Florida, Gainesville, FL 32611, USA*
[5]*Instituto de Astrofisica de Andalucia (CSIC), Glorieta de la Astronomia S/N, E-18008 Granada, Spain*
[6]*National Astronomical Observatory of Japan, Mitaka, Tokyo 181-8588, Japan*

Accepted 2018 January 10. Received 2018 January 9; in original form 2017 August 3

ABSTRACT

We present a polarization map of the warm dust emission from the minispiral in the central parsec of the Galactic Centre. The observations were made at a wavelength of 12.5 μm with CanariCam mounted on the 10.4-m Gran Telescopio Canarias. The magnetic field traced by the polarized emission from aligned dust grains is consistent with previous observations, but the increased resolution of the present data reveals considerably more information on the detailed structure of the B field and its correspondence with the filamentary emission seen in both mid-infrared continuum emission and free–free emission at cm wavelengths. The magnetic field appears to be compressed and pushed by the outflows from luminous stars in the Northern Arm, but it is not disordered by them. We identify some magnetically coherent filaments that cross the Northern Arm at a position angle of ∼45°, and which may trace orbits inclined to the primary orientation of the Northern Arm and circumnuclear disc. In the east–west bar, the magnetic fields implied by the polarization in the lower intensity regions lie predominantly along the bar at a position angle of 130°–140°. In contrast to the Northern Arm, the brighter regions of the bar tend to have lower degrees of polarization with a greater divergence in position angle compared to the local diffuse emission. It appears that the diffuse emission in the east–west bar traces the underlying field and that the bright compact sources are unrelated objects presumably projected on to the bar and with different field orientations.

Key words: dust, extinction – ISM: individual objects: Galactic Centre – Galaxy: centre – galaxies: magnetic fields – infrared: ISM.

1 INTRODUCTION

The central few parsecs of the Milky Way Galaxy host a rich and complex environment, which includes the central cluster of old stars, the 4×10^6 $M_\odot$ black hole, numerous hot mass-losing stars, and a young stellar cluster together with molecular, ionized, and neutral gas mixed with dust (e.g. Genzel, Eisenhauer & Gillessen 2010). Observations of continuum emission at mid-infrared wavelengths trace out emission from warm dust heated by radiation from these numerous sources (Smith, Aitken & Roche 1990; Telesco, Davidson & Werner 1996; Viehmann et al 2006; Lau et al. 2013). The most prominent structure associated with mid-IR emission from warm dust coincides with the so-called minispiral, a quasi-coherent structure seen in radio continuum (free–free emission) (e.g. Gezari & Yusef-Zadeh 1991) and in ionized gas through the 12.8 μm [Ne II] fine structure line (Lacy, Achtermann & Serabyn 1991) and in high-n H recombination lines (Roberts & Goss 1993; Zhao et al 2010). Radial velocity measurements of the minispiral have been used by a number of authors to investigate the kinematics of the ionized gas in order to study the relationship between this material and other components of the Galactic Centre. The Western Arc of the minispiral appears to trace the inner edge of the 1.5–5 pc circumnuclear disc (CND) of molecular material around the Galactic Centre (Serabyn & Lacy 1985). The Northern Arm and at least parts of the east–west bar may coincide with ionization fronts at the interface between an infalling neutral cloud and the ionized gas in the central cavity (Telesco, Davidson & Werner 1996).

The ionized gas kinematics have been fitted by both circular (Serabyn et al 1988; Lacy, Achtermann & Serabyn 1991) and elliptical Keplerian orbits (Paumard, Maillard & Morris 2004; Zhao et al. 2009) around the centre, possibly with an infalling component. Irons, Lacy & Richter (2012) argue that the Northern Arm of the minispiral connects with the Western Arc to trace an Archimedean spiral structure that may be induced by a density wave in the medium. They point out the similarity of the orbital inclinations

⋆ E-mail: p.roche@physics.ox.ac.uk

of the ionized gas in the minispiral to that of the molecular material in the CND. Regardless of the detailed orbital shapes, the minispiral appears to trace the ionized edge of a much larger structure, while the minispiral orbital plane appears to be very similar to that of the CND, suggesting a close relationship and perhaps a common origin. Neutral gas, traced by [O I] emission, fills in the region between the Northern Arm of the minispiral and the north-eastern arc of the CND (Jackson et al. 1993), suggesting a direct relationship between the ionized, neutral, and molecular components in that region. Recent observations with ALMA have shown a complex distribution of clumps emitting a range of molecular lines. While most of the molecular gas emission traces the CND, a number of clumps are detected in the region west of the Northern Arm, north of the east–west bar and extending north and west of SgrA*. The total mass of molecular gas in the central parsec appears to be a small fraction of that in the ionized gas (Moser et al. 2017).

Measurements of the emissive polarization from warm, aligned dust grains at mid-IR wavelengths have been employed to estimate the direction of the component of the magnetic field in the plane of the sky and place some constraints on the likely field strength (Aitken et al. 1991, 1998; Glasse, Aitken & Roche 2003). Spectropolarimetry has allowed the contribution from the absorptive interstellar polarization to be separated from the emissive polarization arising from warm aligned grains in the dusty structures in the minispiral (Aitken et al. 1986). The polarization in the Northern Arm is quite ordered, suggesting that the magnetic field is strong, with a field strength of ∼2 mGauss, and that it lies primarily along the arc of the Northern Arm. Aitken et al. (1998) have argued that the polarization may be saturated in the Northern Arm, such that reductions in percentage polarization are related to the inclination of the field with respect to the plane on the sky; in this way, with the radial velocity measurements of Roberts & Goss (1993), they were able to use the observed polarization to construct a 3D estimate of the kinematics. The polarization in the east–west bar of the minispiral was found to be much less ordered and the relationship between the polarization and radial velocity structures is less clear. The resolution of these observations was diffraction limited to 0.8 arcsec by the primary mirrors of the 4-m Anglo-Australian and UK Infrared telescopes. The data presented here, obtained with the 10.4-m Gran Telescopio Canarias (GTC), provide an improvement in resolution of a factor of 2.

Here, we present 12.5 μm imaging polarimetry of the central 0.75 parsec (at an assumed distance of 8 kpc; Boehle et al. 2016) of the Galactic Centre to investigate the polarization and magnetic structures at higher resolution than previous observations, and in particular to investigate the relationship between the outflow sources and the magnetic field.

2 OBSERVATIONS

The observations were obtained with the CanariCam mid-IR multimode camera (Telesco et al. 2003) mounted on the Nasmyth A platform of the 10.4-m GTC between 2015 July 28 and August 2 in programme GTC6-14AGCAN. CanariCam was used in its dual-beam polarimetric mode (Packham, Hough & Telesco 2005) wherein a Wollaston prism separates the o- and e-rays and the polarization is modulated by a cryogenic CdSe half-wave plate (HWP) installed in the upstream optical path. The Wollaston prism is used in conjunction with a focal plane mask consisting of three slots, each 20 arcsec long × 2 arcsec wide, and separated by 5 arcsec which prevents overlap of the images in the e- and o-rays on the 320 × 240 pixel Raytheon Si:As detector.

The telescope position was offset in steps of 1 arcsec between exposures, with six steps providing full sampling of the field. The Si-6 12.5 μm filter was chosen as it offers good sensitivity and high polarization efficiency while maximizing the emissive polarization component and minimizing the absorptive interstellar polarization (see Section 4.3). The filter bandpass (50 per cent of peak transmission) is 12.08–12.76 μm. Standard chop-nod sequences were used, with the waveplate rotated in sequence by 0°, 22.5, 45°, and 67.5. A chop-throw of 25 arcsec at a position angle (PA) 45° east of north was used to minimize contamination from emission in the reference beam. The pixel size of CanariCam is 0.080 arcsec. Each observing block (OB) consisted of a set of six exposures shifted successively by 1 arcsec in right ascension, each with an on-source integration time of 126 s. As the slots are 2 arcsec wide, each pixel on the sky is exposed for 256 s in each OB. The polarization map presented here is the accumulated signal from three OBs with a total on-source exposure time per pixel of 12.6 min. The Galactic Centre only rises above 2 airmasses for short periods on La Palma, and although the conditions for the observations were good, the low elevation at which they were conducted resulted in the image quality of the final image being ∼0.45 arcsec compared to the diffraction limit of 0.3 arcsec.

A mosaic constructed from the acquisition images taken with CanariCam through the 12.5 μm filter is shown in Fig. 1. This image covers a slightly larger area than that used for the polarimetric observations, and serves as a guide to the positions of the compact emission peaks and other structures discussed below. It also demonstrates the effects of the finite chop used in the polarization measurements. Negative structures in the south-west corner of the image result from chopping on to the Northern Arm, IRS5, and the compact objects further to the east. However, the polarization measurements do not extend as far to the south-west as this region, since the emission is too faint and any emission structure in the chopped beam is at very low levels. The very good agreement with previous observations taken with a range of instruments indicates that contamination from residual emission is not significant. Also shown in Fig. 1 is a cartoon to illustrate the larger scale structures in the central few parsecs of the Galaxy.

3 REDUCTION

The observations were reduced using custom PYTHON routines described in Lopez-Rodriguez et al. (2016). The difference for each chopped pair was calculated and the nod frames then differenced and combined to create a single image for each PA of the HWP. During this process, all images were examined for high or variable background that could indicate the presence of clouds or variable precipitable water vapour, but conditions were good and no data were excluded.

The ordinary (o-) and extraordinary (e-) rays for each HWP PA were extracted for each slot of every data file. The area extracted from each slot is 1.8 arcsec × 20.0 arcsec, slightly undersized compared to the physical slots to avoid vignetting and edge effects. Observations at consecutive telescope pointings provided overlap of the slots by about half their width, and the common areas are used for registration in construction of the final mosaic. For each slot of every file, the o- and e-rays, produced by the Wollaston prism, were used to calculate the Stokes parameters I, Q, and U according to the ratio method. The percentage polarization is then $P^2 = (Q^2 + U^2)/I^2$ and PA = 0.5 arctan (U/Q). The images were checked for consistency in the polarimetric observations between slots, files, and OBs. Aperture photometry and polarimetric measurement of the

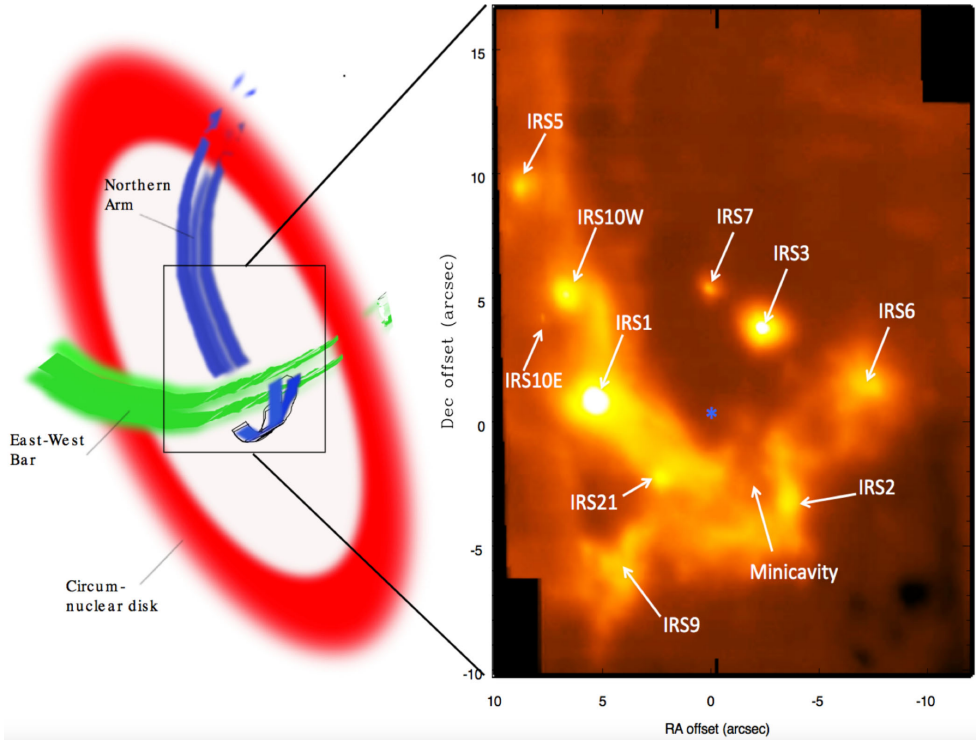

Figure 1. Right: 12.5 μm acquisition image mosaic. The positions of several of the bright compact emission peaks discussed in the paper are indicated. Offsets are relative to the position of SgrA*, which is indicated by a star. Left: cartoon showing the larger scale structures in the central 5 pc and their relation to the features discussed in the text.

brightest objects in the slots were performed for every OB, which yielded variations smaller than 5 per cent in the Stokes parameters I, Q, and U.

CanariCam was mounted on the Nasmyth A platform where the tertiary mirror produces significant instrumental polarization (IP). The IP was determined during CanariCam commissioning, and a prescription is provided on the GTC website[1]. Specifically, the IP is $P_{ins} = 0.6 + / - 0.2$ per cent with a dependence on the PA of polarization given by $PA_{ins} = -(RMA+Elev) - 29.^{\circ}6$, where RMA is the Nasmyth rotator mechanical angle and Elev is the telescope elevation; $29.^{\circ}6$ is the latitude of the observatory site.

The IP was corrected as follows. The normalized Stokes parameters, $q_{ins} = Q_{ins}/I_{ins}$ and $u_{ins} = U_{ins}/I_{ins}$, of the IP were computed using the above prescription for the degree P_{ins} and position angle PA_{ins} of the IP. Then, q_{ins} and u_{ins} were subtracted from the normalized Stokes parameters of the Galactic Centre images. The polarization efficiency was corrected based on data provided by the GTC website, using the quoted polarization efficiency of 88.3 per cent at 12.5 μm. For each OB, mosaics were constructed for each slot, taking into account the 1 arcsec offsets between them. The images through each slot were interpolated to 1/4 pixel, offsets of 1 arcsec were applied to the slots and finally slots were co-added.

The final mosaic of the Galactic Centre was constructed by combining the I, Q, and U images for each OB. The images were resized and the mosaics from each OB were registered and shifted to a common pixel, and finally co-added. The required 0.5–2 pixel shifts required are below the typical full width at half-maximum of 0.45 arcsec. By ensuring that exactly the same offsets are applied to the I, Q, and U images through the slots, the polarization fidelity of the CanariCam instrument is preserved, even if the spatial positioning has some errors.

As a final check on consistency, aperture photometry and polarimetric measurements of prominent features in the images were performed. Variations of the total flux counts at a level of 2 per cent were found, but all images show consistent polarimetric maps, and the final measured polarizations are in agreement with literature values.

4 CALIBRATION

4.1 PA calibration

The compact polarized young stellar object AFGL 2591 was used as a PA calibrator. It is a bright, highly polarized object with $P = 4.5 \pm 0.1$ per cent at 11.6 μm, and a wavelength-independent PA across the 8–13 μm window of $170 \pm 1^{\circ}$ (Aitken et al. 1988). Observations of AFGL 2591 were made at several positions in the slot mask to check the calibration across the CanariCam Field. No significant variations were detected, and the average $P = 4.7 \pm 0.1$ per cent at PA$= 44.9 \pm 1.^{\circ}0$. Our measured degree of polarization is in good agreement with those published by Aitken et al. (1988) and Smith et al. (2000). Comparison of the CanariCam measurements to the literature values indicates a zero-angle correction of $\Delta PA = 125.1 \pm 1.^{\circ}0$, and this correction was applied to all of the observations.

4.2 Unpolarized standard

Brief observations of a bright, and assumed unpolarized star, 37 Sgr (HD175775), were made to provide estimates of the point spread function (PSF) and the IP. 37 Sgr was observed in the middle of

[1] see http://www.gtc.iac.es/instruments/canaricam

each slot and the data were reduced following the same procedure employed for the Galactic Centre. After correction for the IP outlined above, the average residual percentage polarization was $P = 0.24 \pm 0.09$ per cent indicating that the correction is stable and that the prescription is appropriate. The observations of AFGL 2591 and 37 Sgr were made on different nights from the observations of the Galactic Centre, and so they cannot be used as fiducial PSF references for the Galactic Centre observations, while the flux calibrations are subject to substantial uncertainties.

4.3 Correction for interstellar polarization

The measured polarization in the Galactic Centre arises from a combination of polarized emission from warm, aligned dust grains in the central parsec together with an interstellar absorptive polarization component produced by dichroic absorption by cool, aligned grains in the interstellar medium between the Earth and the Galactic Centre (Aitken et al. 1986). In order to reveal the intrinsic emissive polarization, correction for the absorptive component is required. The absorptive interstellar polarization component has been estimated by unfolding emissive and absorptive components from spectrophotometric observations across the silicate feature between 8 and 13 μm, and by measuring the polarization in the 12.8 μm [Ne II] emission line, which is assumed intrinsically unpolarized (Aitken et al. 1986). The isolated compact source IRS3 shows no indication of emissive polarization, with a constant PA across the *N* band and a polarization profile compatible with the narrow silicate absorption profile found in lines of sight towards the Galactic Centre and other sightlines in the interstellar medium (Roche & Aitken 1984, Roche & Aitken 1985, Bowey, Adamson & Whittet 1998). These analyses indicate that the absorptive component is broadly constant across the central parsec, and is well modelled by the polarization curve derived from the measurements of IRS3 by Smith et al. (2000).

There is evidence of patchy extinction towards sources in the central regions of the Milky Way. In particular, extinction increases markedly in the northern and southern lobes of the CND (e.g. Scoville et al. 2003; Lau et al. 2013), but although the extinction within the central parsec may be enhanced in some areas, it appears that the interstellar component of the extinction towards the bright emission regions discussed here is not subject to large variations. For example, Moultaka et al. (2004) find that the variation over the central 0.5 pc is $\Delta A_K \leq 0.5$ mag, while Schödel et al. (2010) find that the distribution of extinction derived from *H*–*K* band colours is characterized by $A_{Ks} = 2.74 \pm 0.3$ mag. Chatzopoulos et al. (2015) estimated that the extinction by dust within the central few parsecs (e.g. caused by the minispiral) is typically of the order of A_K ∼0.4 mag and probably less than half that in the region studied here. Similarly, Roche & Aitken (1985) found relatively small variations in the mid-IR absorption optical depth towards the bright compact sources in the central parsec. It therefore appears safe to conclude that the likely variation in the interstellar absorptive component of polarization at 12.5 μm in the region considered here is less than 0.1 per cent.

The interstellar absorptive polarization is discussed in detail by Aitken et al. (1991, 1998), who compare estimates of the interstellar polarization from mid-infrared spectropolarimetry and imaging polarimetry and conclude that all of the results are consistent with a constant polarization of 1.8 per cent at PA$= 5 \pm 5^\circ$ at 12.5 μm. Spectropolarimetry of the isolated dusty supergiant IRS3 (Aitken et al. 1986) has demonstrated that it has no emissive component of polarization but that it is representative of the interstellar absorptive component to the Galactic Centre. The measured polarization of IRS3 in the current data is 1.7 per cent at PA ∼10° and we have used this value to correct for interstellar polarization. On the assumption that IRS3 is intrinsically unpolarized, this approach corrects for any residual IP as well as the interstellar absorptive component. As pointed out by Aitken et al. (1998), errors of a few degrees in PA only affect the resultant emissive polarization at the tenth of a per cent level. In making the correction in this way, the polarization on IRS3 is forced to be zero, but it is noteworthy that the residual polarization of the other prominent isolated supergiant IRS7 is less than 1 per cent, suggesting that this object too has a low intrinsic polarization, and giving confidence that the correction applied is appropriate across the field.

The final polarization image after correction for interstellar polarization, and with the vectors rotated by 90° to indicate the direction of the magnetic field is shown in Fig. 2. The polarization vectors are displayed at intervals of 0.24 arcsec, i.e. with bins of 3 × 3 detector pixels to allow the vector patterns to be seen more clearly and to improve the signal-to-noise ratio per pixel in the lowest flux regions. The resulting vector maps are oversampled by a factor of ∼2 with respect to the image resolution. The offsets in the polarization image are with respect to the position of SgrA*, taken as RA = 17:45:40.04, Dec. = −29:00:28.17 (Reid & Brunthaller 2004).

5 INTERPRETATION OF POLARIZATION

Because of dissipative effects in grains spinning in a magnetic field, *B*, the grains will tend to align such that the grain spin axis is parallel to its maximum moment of inertia. The grain spin axis will precess around the magnetic field direction, providing a net alignment of an ensemble of non-spherical dust grains such that the grain long axes are preferentially aligned perpendicular to the *B* field direction (see e.g. Andersson, Lazarian & Vaillancourt 2015, for a review). This produces polarized emission with the PA normal to the *B* field, so that the vectors, when rotated by 90°, trace out the component of the field directions in the plane of the sky. The aspect ratios and detailed composition and properties of the emitting grains or the alignment mechanisms in the Galactic Centre are not known, so it is not possible to derive quantitative estimates of the field strength. However, indirect arguments (see Aitken et al. 1998) indicate that the minimum field strength in the bright regions is 2 mGauss.

The magnetic field vectors indicated by the polarization measurements presumably reflect the effects of orbital motion and shear coupled with the impacts of outflows from stars in the central regions, together with possible infall. Previous observations (Aitken et al. 1991, 1998; Glasse, Aitken & Roche 2003) have shown that the 12.5 μm polarization vectors trace out coherent field structures in the Northern Arm with continuous and slowly varying degrees of polarization, suggesting that the field is oriented primarily in the plane of the sky and may be amplified by shearing motions as the material orbits the centre of the Galaxy. On the other hand, other researchers (e.g. Irons, Lacy & Richter 2012) have argued that the gas does not move along the streamers, but rather that the prominent Northern Arm structure is produced by orbital precession of gas in circular orbits producing a density wave, together with the enhanced ionizing flux from the sources in the central region. It may be that some of the bright filamentary structures are enhanced by compression by outflowing gas and that they trace ionization fronts at the interfaces of the warm material and hot gas.

We note that some alignment mechanisms, such as radiative torques acting on grains might be expected to lead to greater alignment and higher polarization in regions with high radiation fluxes (e.g. Andersson, Lazarian & Vaillancourt 2015). This does not

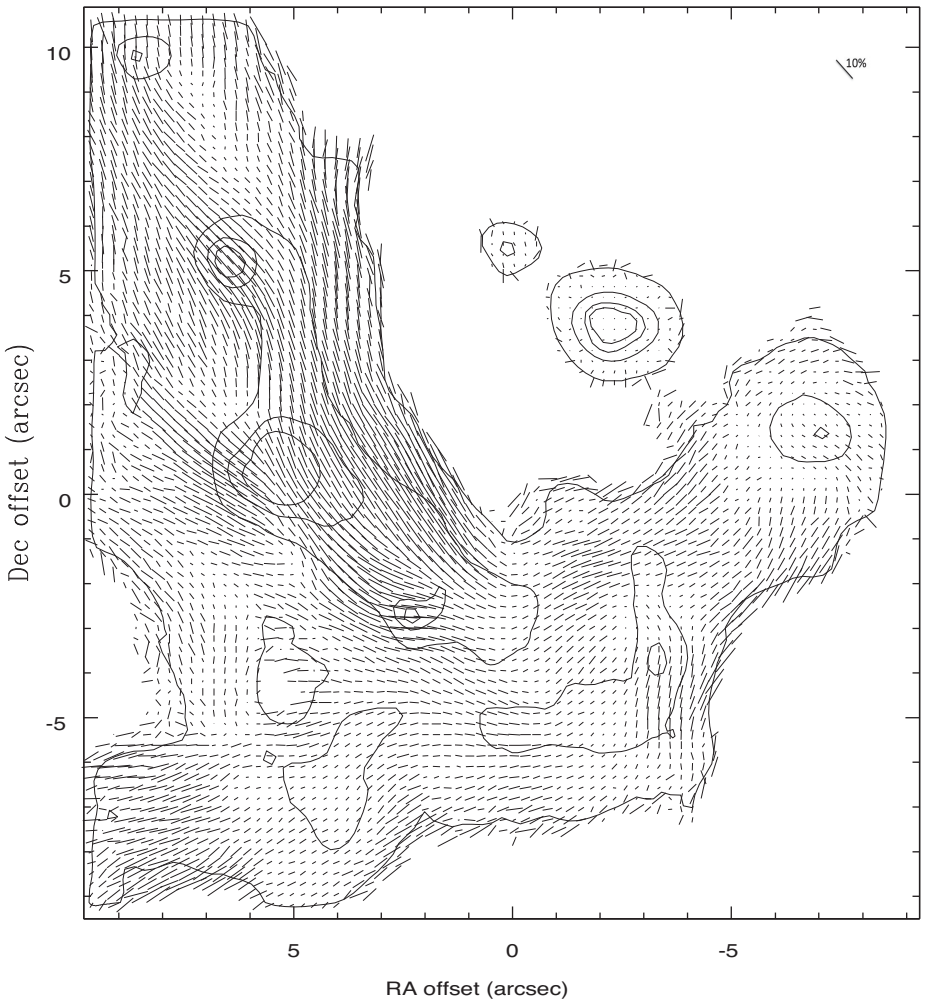

Figure 2. The emissive polarization map of the central 0.74 × 0.78 pc of the Galaxy. The length of the polarization vectors is proportional to the percentage polarization, with the scale indicated at the upper right. The vector PAs have been rotated by 90° so that they point along the inferred magnetic field directions in the plane of the sky. A flux threshold has been applied to prevent large and spurious vectors from being plotted. A few contours of intensity are shown to allow registration against the image and the positions of the compact sources identified in Fig. 1. As explained in Section 4.2, the flux calibration is uncertain, but the lowest contour is at approximately 1 Jy arcsec^{-2}, with further contours at ∼3, 6, and 9 Jy arcsec^{-2}. Offsets are in arcsec relative to the position of SgrA*.

appear to be the case in the central region of the Milky Way, but Aitken et al. (1998) proposed that the grain alignment may be saturated and that variations in the degree of polarization along the Northern Arm reflect changes in the orientation of the field with respect to the line of sight.

The current results are in agreement with the previously published mid-IR polarization data, and especially with the most recent results which were presented by Glasse, Aitken & Roche (2003); there is excellent agreement between the two data sets but the higher resolution of the current observations reveal new details in the polarization structure.

6 POLARIZATION STRUCTURES

The warm dust emission observed in the mid-infrared lies within the CND traced by molecular lines and far-infrared dust emission. The emissive polarization from dust in the CND has been measured at far-infrared and submillimetre wavelengths (Hildebrand et al. 1993; Novak et al. 2000) at resolutions of ∼40 and 20 arcsec, respectively, and indicates that the fields in the CND generally lie in the north–south direction, possibly resulting from wind-up of a poloidal field by the CND rotation.

The inferred magnetic field in the region of the Northern Arm north of IRS5 is also primarily north–south and is well ordered, consistent with the field lying in the direction of the orbital motion (Aitken et al. 1991, 1998; Glasse, Aitken & Roche 2003). However, inspection of the data presented in Fig. 2 shows that the structure is more complex in the central 0.5 parsec. The complexity of the structures and the regions with coherent vectors can be more readily appreciated in Fig. 3. This figure has been produced with a line integral convolution algorithm (Cabral & Leedom 1993) which highlights the flow of the field and its filamentary structure in the minispiral, but apparently converging south of SgrA*.

In Fig. 4, we have drawn lines to indicate regions of coherent vectors, while circles are drawn at the positions of low polarization or null points. The lines are drawn by hand and indicate regions that appear to have common or slowly changing polarization structures. In the Northern Arm, regions of north–south vectors are found at the top of the figure and also just above the east–west bar; these are indicated in green and may represent the overall field in the Northern

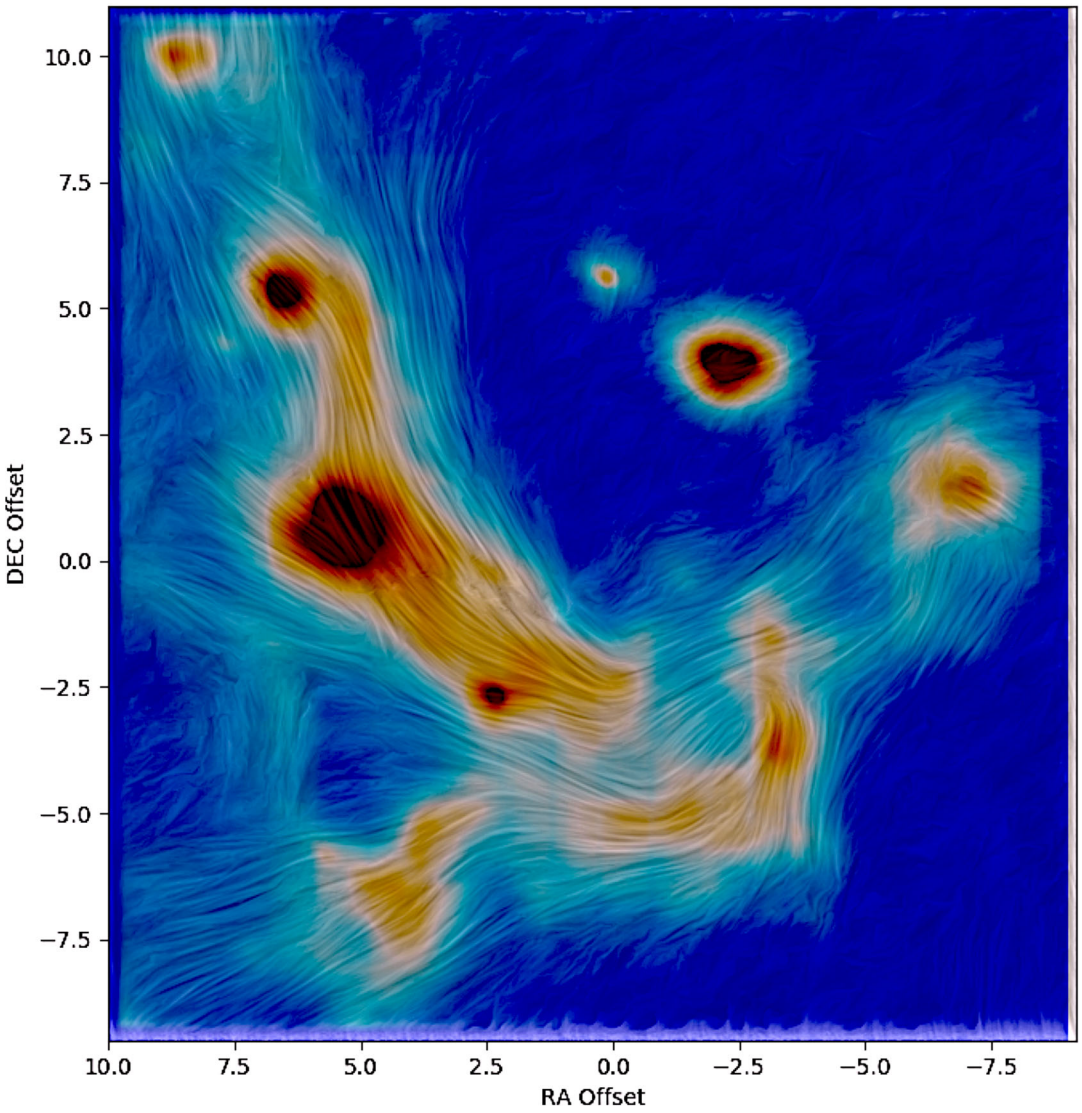

Figure 3. The polarization map of the central 0.75 parsec produced with a line integral convolution to emphasize the coherent structures.

Arm. Other regions in the Northern Arm show coherent structures that are predominantly north–south on the western rim, but rotating towards 45° as the vectors are traced to the south. South and east of IRS1, vectors trace out structures with field directions close to 45°. A run of vectors connects the bright peaks IRS5, IRS10W, IRS1, and IRS21, suggesting that these sources are linked by a coherent field. In contrast, many regions in the east–west bar show coherent structures with PA ∼120°–140°, following the overall direction of the E–W bar. As found previously, the strong ordered vectors in the Northern Arm become less defined and appear to curve below and perhaps wrap around SgrA*, while the degree of polarization decreases markedly in regions to the west of SgrA*.

The improved resolution of the data presented here allows us to identify regions of low polarization. These regions are indicated by circles in Fig. 4 and they generally occur at positions where two coherent structures with different PAs intersect. For example, the circle to the south-west of IRS5 indicates a null point that occurs where the general N–S field of the Northern Arm intersects with the field that links the bright compact IRS sources along the intensity ridge. Similarly, a low or null point occurs to the north-east of IRS1, where a stream of vectors at PA ∼45° intersects with a north–south structure along the ridge linking IRS1 and IRS10W. It appears that a number of polarized filaments oriented at about 45° are superimposed upon the overall N–S run of the magnetic field in the diffuse emission in the Northern Arm. The most prominent of these features are indicated by the regions that lie between the thick coloured lines drawn in Fig. 4. A similar situation may prevail in the east–west bar where regions with field directions oriented approximately N–S (e.g. south of IRS2) stand out against the dominant field directions with PA ∼130° in the diffuse material along the bar.

6.1 The compact sources

The polarization of the compact IRS sources measured in 6 pixel (0.48 arcsec) diameter apertures is listed in Table 1. The maximum levels of polarization are found in the region of the Northern Arm to the east of SgrA* (listed as NA Rim in the table) and towards the ridge between IRS1 and IRS21, where the polarization reaches 12 per cent. The polarization of the compact sources is similar to, but generally at somewhat higher levels and rotated in angle by a few degrees compared to previous measurements (Aitken et al. 1986), reflecting the fact that the small apertures used here integrate

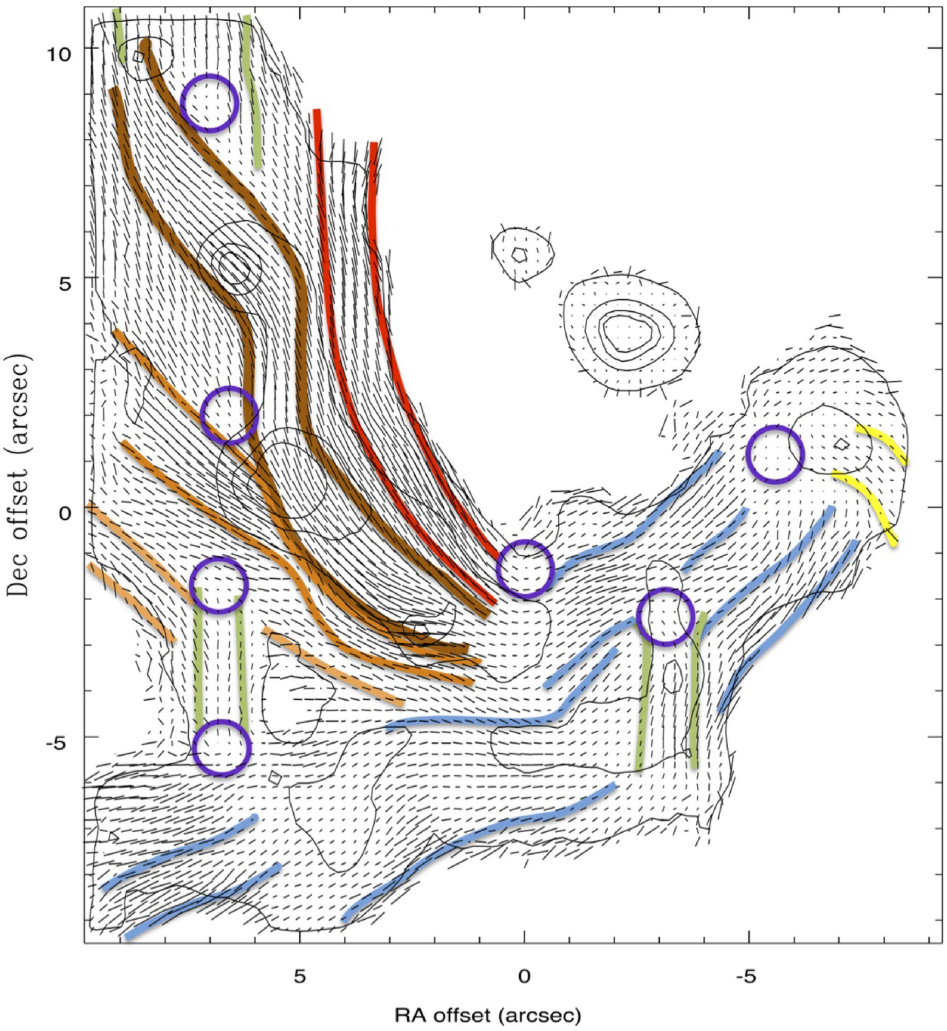

Figure 4. The polarization map of the central 0.75 parsec from Fig. 2 overlaid with lines to indicate regions with coherent field structures. Red and brown lines indicate regions of coherent vector orientations on the inner edge of the Northern Arm and in the regions of the compact objects IRS5, IRS10W, IRS1, and IRS21. Green lines indicate north–south structures, possibly related to the bulk Northern Arm field, while blue lines trace coherent structures along the east–west bar. Purple circles indicate null points in the polarization, and generally occur where two coherent polarization structures at different orientations are superposed.

Table 1. Emissive polarization and PA measured in 0.48 arcsec diameter apertures. Offsets are with respect to SgrA*.

Aperture polarization measurements					
Position	Offset (arcsec) RA	Dec.	Flux density Jy	P per cent	θ °
IRS1	5.2	0.6	9.47	8.1	113.6
IRS2	− 3.4	− 3.6	2.59	2.5	85.1
IRS5	8.6	9.9	2.43	4.8	94.1
IRS7	0.0	5.6	1.44	0.9	99.3
IRS10W	6.5	5.3	4.76	9.6	130.2
IRS10E	7.7	4.2	0.86	3.9	108.5
IRS21	2.3	− 2.8	3.72	10.2	87.3
NA Rim	2.3	0.2	0.87	12.1	121.1

over smaller areas, better isolating the emission from the compact objects, and reducing PA variations within the aperture. The polarization angles listed in Table 1 are the measured PAs of the intrinsic emission, i.e. they have not been rotated to indicate the field directions. The flux densities listed are simply the integrated flux within the aperture, with no correction for underlying diffuse emission. Comparisons with previous estimates of fluxes are difficult because of the small aperture sizes used here and because most

published measurements are corrected for interstellar extinction and diffuse background emission (e.g. Viehmann et al 2006). Furthermore, the flux calibration was applied from observations of 37 Sgr made on the night before the Galactic Centre polarization observations, so that while the relative fluxes will be more accurate, the absolute uncertainties are probably at least 20 per cent, and the flux estimates assume that the PSF is similar to that of 37 Sgr.

In general, these measurements emphasize the lack of perturbation of the field by the compact sources. However, there does appear to be dilution of the polarization at the position of IRS10E. IRS10E is visible in Fig. 1 and more prominently in Fig. 3 as a relatively weak compact object approximately 1.5 arcsec south-east of the prominent Northern Arm object IRS10W. At this position, there is a reduction in percentage polarization by a factor of ∼2 relative to the surrounding areas, but the PA appears unaffected, consistent with dilution resulting from inclusion of unpolarized flux in the beam. This is consistent with IRS10E being an unrelated object, separated from the Northern Arm along the line of sight; it is the closest OH-IR star to SgrA* (Lindqvist et al. 1992) and has a compact morphology unlike those of the bow-shock sources (Sanchez-Bermudez et al. 2014).

6.2 The Northern Arm

The polarization pattern revealed in these data is complex. It appears that a number of magnetic filaments are superimposed on the larger scale N–S field. It is striking that the fields do not appear to be randomly distributed, but rather have orientations that are clustered around distinct PAs. For example, in the parts of the Northern Arm east of SgrA* and north of IRS21, the field directions are essentially confined to orientations between 0° and 60° with subregions on scales of 1–2 arcsec with much more restricted ranges in PA.

It is especially noteworthy that, in agreement with the earlier results of Aitken et al. (1991, 1998), and with the exception of IRS10E discussed above, the degree of polarization is unaffected by the intensity peaks, with no evidence of dilution or major disruption of the local field. This is demonstrated at higher resolution in the present data. The objects associated with the mid-IR intensity peaks are well studied and appear to be embedded stars with large mass-loss rates (Tanner et al. 2005; Sanchez-Bermudez et al. 2014). The fact that the warm dust associated with the stars is aligned with the same orientation as the diffuse emission in the ridge, and that there is no dilution of polarization by unpolarized or differently oriented polarized circumstellar emission from the stars indicates that they are embedded within the magnetic field lines. In general, the grain alignment to the magnetic field is a property of the diffuse emission rather than the intensity peaks. The intensity peaks do not appear to have any significant impact on the degree of polarization, although the fact that the bright peaks are linked by coherent field structures suggests that the embedded stars may distort the run of the magnetic field flux tubes on scales of ∼0.1 pc. It seems that the outflows from the stars do not overcome the magnetic field, but rather may compress and shift the field lines.

Figs 3 and 4 suggest several structures reminiscent of flux tubes. The coherent vectors with uniformly high degrees of polarization linking the bright IRS sources from IRS5 at the top of the image through IRS10W, IRS1, and IRS21 before merging into the east–west bar define the most prominent structure; this is indicated by the brown thick lines in Fig. 4. High-resolution images of these bright compact objects (e.g. Tanner et al. 2005; Buchholz et al. 2013; Sanchez-Bermudez et al. 2014) reveal bow-shock structures that indicate that the outflows from these embedded stars are interacting directly with material in the Northern Arm. The exact nature of these stars is not clear because their spectra reveal few diagnostics, but it appears that they may be Wolf–Rayet stars with high mass-loss rates (Tanner et al. 2005). We can estimate the impact of those outflows on the filaments: the energy in the magnetic field is $B^2/2\mu \sim 210^{-7}$ erg cm^{-3}, but the ram pressure from an outflow from a star at a distance of 0.01 pc (0.25 arcsec) with a mass-loss rate of 10^{-5} $M_\odot$ yr^{-1} and an outflow velocity of 200 km s^{-1} is more than an order of magnitude greater. As discussed above, the absence of perturbation in the polarization pattern in the local field indicates that the stars must be embedded in the polarized material and so the separation between the stars and the diffuse polarized material must be small. The estimates of ram pressure and magnetic energy suggest that the stellar outflows can compress and push the field lines, consistent with the patterns seen in the polarization vectors in Fig. 2 and in the high-resolution near-infrared polarization images of Buchholz et al. (2013).

Two coherent structures, indicated by the thick light brown lines in Fig. 4, cross the southern part of the Northern Arm with orientation and polarization vectors at PA ∼45°. One of these appears to flow from the north-east to intersect with the structure linking the bright IRS sources just to the east of IRS1 where there appears to be a convergence of flux tubes, and then continues at a similar PA to the south-west. To the east of IRS1, the coherent field appears to join on to a short bright emission filament at the same PA in the radio continuum image in Fig. 5 and then either runs parallel to or merges with the ridge of emission linking the IRS sources. A second less defined structure is apparent, approximately 4 arcsec south of this but this becomes indistinct in Fig. 4 after it meets a structure with N–S vectors above the east–west bar and is more clearly seen in Fig. 3. These structures could represent filaments lying, and perhaps tidally stretched, along orbits around SgrA*, but inclined to the predominantly N–S directions of the brightest parts of Northern Arm (see e.g. the discussions by Irons, Lacy & Richter 2012; Paumard, Maillard & Morris 2004, and fig. 8 in the latter). If the magnetic fields do trace the orbits of streamers, sensitive measurements of a more extended area might permit the estimation of orbital parameters.

The region of highest emissive polarization is the part of the Northern Arm directly east of SgrA*. Here, the polarization reaches a maximum of 12 per cent, which is the highest value of dust polarization detected in the mid-IR to date. As discussed by Aitken et al. (1998), if the alignment is saturated, the variations of polarization may reflect the orientation of the field with respect to the line of sight. The measurements presented here suggest that the maximum polarization is somewhat higher than discussed by Aitken et al. (1998), but they confirm the conclusion that the region of the Northern Arm south and west of IRS1 may lie close to the plane of the sky.

In Fig. 5, the polarization vectors are overlaid on the 1.3 cm radio emission map of Zhao et al. (2009). There is a general but not detailed correspondence between the radio structures and the mid-IR emission, but the higher resolution of the former reveals additional structure. In particular, Zhao et al. (2009) in their fig. 22 have drawn attention to an apparently helical structure seen most prominently in the region west of IRS5, which they propose may indicate instabilities in a hydromagnetic flow. This region north of IRS10W coincides with an area of low 12.5 μm polarization, and with the northernmost null region in Fig. 4. The null region could mark a turning point in the helical structure, where the projected magnetic field has a sharp change of direction. The polarization of the loop in the structure immediately north of IRS10W is

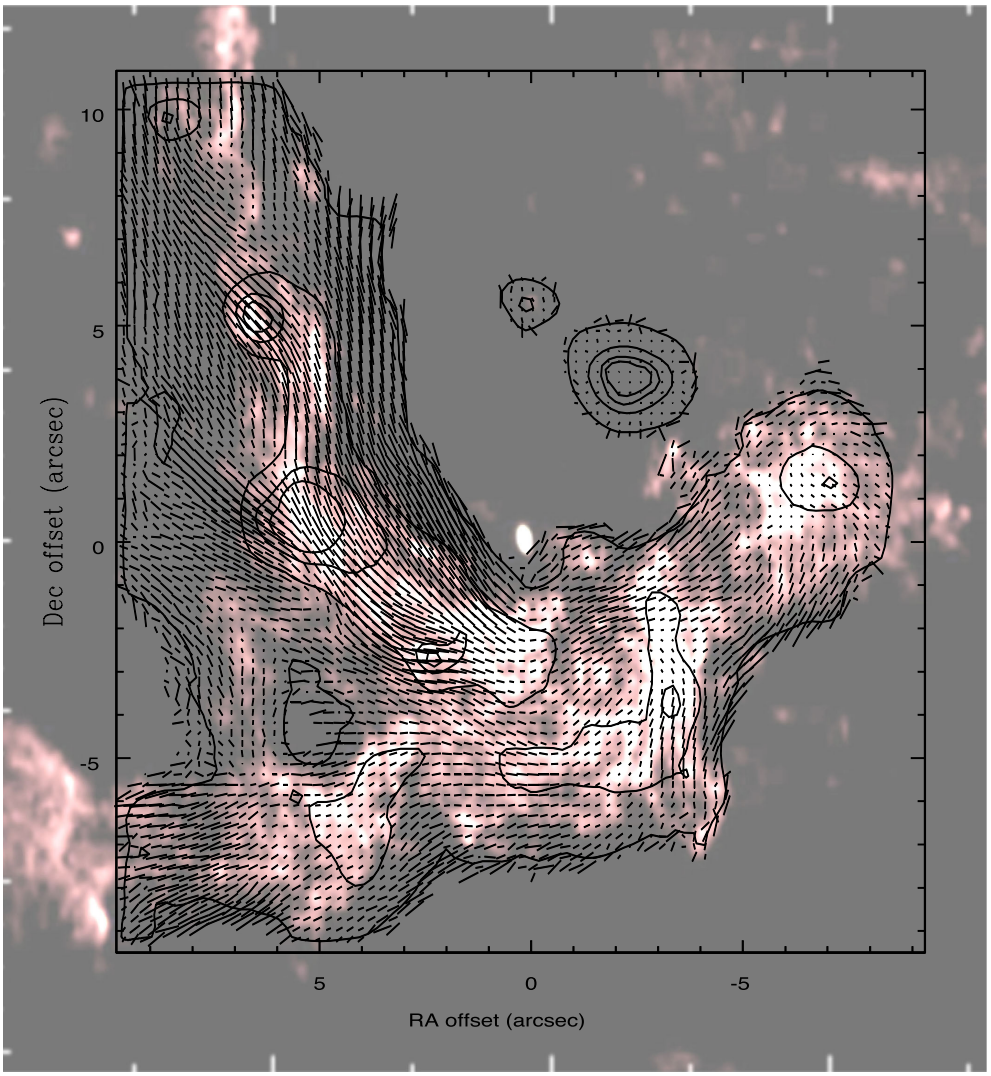

Figure 5. The polarization map superimposed on the 1.3 cm radio map of Zhao et al. (2009) displayed as a grey-scale, and reproduced with permission of the AAS. The radio image has been aligned manually to the mid-IR intensity images; the image registration will not be precise, with estimated uncertainties of 0.1 arcsec.

significantly lower than that in the loop further to the north and above the null region. If the field directions follow the turns in the loop, we would expect a decrease in the net polarization in the region immediately south-west of the null region where the angle of $\sim 45^\circ$ is not aligned to the general north–south field of the Northern Arm. The polarization does indeed decrease there, but also stays low as the loop orientation changes to north–south. There are several possible explanations for reduced polarization along the loop; for example, it could result from dilution by emission from a region where the field orientation changes from the plane of the sky to along the line of sight. High-resolution polarization observations of the region north of IRS5 would enable us to follow the helical structure in more detail and unravel the polarization properties.

6.3 The east–west bar

In Fig. 5, it is apparent that the polarization in the lower intensity regions of the east–west bar has vectors pointing approximately along the bar and are in general more strongly polarized than the regions with higher radio intensity. This is especially obvious in the regions to the east and to the south-west of IRS9, the region between SgrA* and IRS2, including part of the minicavity, and the region between IRS2 and IRS6. These areas of high polarization and with vectors aligned along the bar are delineated by the blue lines in Fig. 4. The behaviour of the polarization in the east–west bar is quite different from that in the Northern Arm; in the latter, the bright sources do not appear to affect the degree or PA of polarization. The lower levels of polarization in the bright areas in the east–west bar could result from dilution by emission from unpolarized sources or by sources with different polarization PAs.

South of IRS2, the brightest region in the east–west bar, the polarization vectors are predominately north–south (indicated by the green lines in Fig. 4). This region, where the gas shows strongly blue-shifted emission (Zhao et al. 2009; Irons, Lacy & Richter 2012), is often viewed as a continuation of the Northern Arm. Models suggest that the material comprising the main structure of the Northern Arm lies behind SgrA*, but that it loops to the south and west and re-emerges on the near side near IRS2 (Zhao et al. 2009; Irons, Lacy & Richter 2012). The very different orientation of the polarization vectors in this region is consistent with the region

around IRS2 being quite distinct from the general structure of the east–west bar, and the ordered field lines suggest that a substantial component of the field lies in the plane of the sky.

Regions of low polarization in the region around IRS6 in the western part of the bar may result from the superposition of polarized emission with orthogonal directions to the general vector directions where the Western Arc crosses the bar. A small area with polarization vectors at PA$\sim$45° is indicated in yellow in Fig. 4, which may arise in material associated with the Western Arc.

7 CONCLUSIONS

The 12.5 μm polarization image presented here reveals details of the magnetic field in the central 0.75 parsec of the Galactic Centre.

1. In agreement with previous observations, the mid-IR polarization is found to be a property of the diffuse emission rather than the compact, bright sources.

2. In the Northern Arm, a coherent field structure links the bright embedded stars IRS5, IRS10W, IRS1, and IRS21 and continues south and west of SgrA*. The embedded objects do not significantly perturb the inferred magnetic field directions in the immediate vicinity and do not dilute the measured degree of polarization, suggesting that the stars are embedded within the field. However, the fact that the most prominent and brightest objects are linked by a coherent run of vectors suggests that the field has been compressed and aligned to the sources by the stellar outflows.

3. The maximum polarization of 12 per cent at 12.5 μm is found in the Northern Arm east of SgrA*. This may indicate that the magnetic field lies close to the plane of the sky in this region and may represent the maximum polarization produced by the grains.

4. Other coherent field structures are oriented at PA$\sim$45° so that they cross the general run of the Northern Arm. One of these appears to converge with the polarized ridge structure near IRS1, following a filament visible at radio frequencies. These filaments may represent materials on orbits with different inclinations to the bulk of the Northern Arm.

5. In contrast to the Northern Arm, the polarization in the high-intensity regions of the east–west bar is generally lower than in the lower intensity regions, while the PAs also deviate from those in the surrounding diffuse material. It appears that the low-intensity regions trace the predominant magnetic field directions, which run along the bar (with PA $\sim$130°), but that the polarization is diluted or disrupted in the bright regions. It seems that the bright structures in the east–west bar are not embedded in the larger scale east–west magnetic field in the same way as the sources in the Northern Arm are embedded in their magnetic filament. In the western part of the bar, the polarization may be diluted by the superposition of fields from material associated with the Western Arc at PA $\sim$45°, while the emergence of the southern extension of the Northern Arm may account for the region of north–south vectors south of IRS2.

6. A helical structure identified by Zhao et al. (2009) and proposed to arise through instabilities in a magnetic medium appears to have some effect on the polarization vectors. For example, the projected turning point of a loop in the helix coincides with a null in polarization. More coverage of this structure to the north of the present image would allow a more detailed comparison and an investigation of the field directions.

ACKNOWLEDGEMENTS

This paper is based on observations obtained with the GTC, installed in the Spanish Observatorio del Roque de los Muchachos of the Instituto de Astrofisica Canarias, in the island of La Palma. We are very grateful to the support staff, and particularly to the dedicated help of Carlos Alvarez, who provided excellent support and ensured that good-quality data were obtained. We are also grateful to the whole CanariCam team for their skill in delivering a cryogenically cooled dual beam mid-IR imager-spectrometer-polarimeter. CMT acknowledges support for this research from NSF awards AST-0903672, AST-0908624, and AST-1515331.

REFERENCES

Aitken D.K., Roche P. F., Bailey J. A., Briggs G. P., Hough J. H., Thomas J. A., 1986, MNRAS, 218, 363
Aitken D. K., Roche P. F., Smith C. H., James S. D., Hough J. H., 1988, MNRAS, 230, 629
Aitken D. K., Gezari D., Smith C. H., McCaughrean M., Roche P. F., 1991, ApJ, 380, 419
Aitken D. K., Smith C. H., Moore T. J. T., Roche P. F., 1998, MNRAS, 299, 743
Andersson B-G, Alazarian A., Vaillancourt J. E., 2015, ARA&A, 55, 501
Boehle A. et al., 2016. ApJ, 830, 17
Bowey J. E., Adamson A. J., Whittet D. C. B., 1998. MNRAS, 298, 131
Buchholz R.M, Witzel G., Schödel R., Eckart A., 2013, A&A, 557, 82
Cabral B., Leedom L., 1993, Proc SIGGRAPH, Proc. 20th Annual Conf. Computer Gaphics and Interactive Techniques. ACM, New York, p. 263
Chatzopoulos S., Gerhard O., Fritz T. K., Wegg C., Gillessen S., Pfuhl O., Eisenhauer F., 2015, MNRAS, 453, 939
Genzel R., Eisenhauer F., Gillessen S., 2010, Rev. Mod. Phys., 82, 312
Gezari D., Yusef-Zadeh F., 1991, in Elston R., ed., ASP Conf. Ser. Vol. 14, Astrophysics with Infrared Arrays. Astron. Soc. Pac., San Francisco, p. 214
Glasse A.C.H., Aitken D.K., Roche P.F., Astron. Nachr., 324, 3
Hildebrand R. H., Davidson J. A., Dotson J., Figer D. F., Novak G., Platt S. R., Tao L., 1993. ApJ, 417, 565
Irons W. T., Lacy J. H., Richter M. J., 2012, ApJ, 755, 90
Jackson J. M., Geis N., Genzel R., Harris A. I., Madden S., Poglitsch A., Stacey G. J., Townes C. H., 1993, ApJ, 402, 173
Lacy J. H., Achtermann J. M., Serabyn E., 1991, ApJ, 380, 71
Lau R. M., Herter T. L., Morris M. R., Becklin E. E., Adams J. D., 2013, ApJ, 775, 37
Lindqvist M., Winnberg A., Habing H. J., Matthews H. E., 1992, A&AS, 92, 43
Lopez-Rodriguez E. et al., 2016, MNRAS, 458, 3851
Moser L. et al., 2017, A&A, 603, 68
Moultaka J., Eckart A., Viehmann T., Mouawad N., Straubmeier C., Ott T., Schödel R., 2004, A&A, 425, 529
Novak G., Dotson J. L., Dowell C. R., Hildebrand R. H., Renbarger T., Schleuning D. A., 2000, ApJ, 529, 241
Packham C., Hough J. H., Telesco C., 2005, in Adamson A., Aspin C., Davis C. J., Fujiyoshi T., eds, ASP Conf. Ser. Vol. 343, Astronomical Polarimetry: Current Status and Future Directions. Astron. Soc. Pac., San Francisco, p. 38
Paumard T., Maillard J.-P., Morris M., 2004, A&A, 426, 81
Reid M. J., Brunthaler A., 2004, ApJ, 616, 872
Roberts D. A., Goss W. M., 1993, ApJS, 86, 133
Roche P. F., Aitken D. K., 1984, MNRAS, 208, 481
Roche P. F., Aitken D. K., 1985, MNRAS, 215, 425
Sanchez-Bermudez J., Schödel R., Alberdi A., Muzic K., Hummel C. A., Pott J.-U., 2014, A&A, 567, 21
Schödel R., Najarro F., Muzic K., Eckart A., 2010, A&A, 511, A18
Scoville N. Z., Stolovy S. R., Rieke M., Christopher M. H., Yusuf-Zadeh F., 2003, ApJ, 594, 294
Serabyn E., Lacy J. H., 1985, ApJ, 293, 445
Serabyn E., Lacy J. H., Townes C. H., Bharat R., 1988, ApJ, 326, 17
Smith C. H., Aitken D. K., Roche P. F., 1990, MNRAS, 246, 1
Smith C. H., Wright C. M., Aitken D. K., Roche P. F., Hough J. H., 2000, MNRAS, 312, 327

Tanner A., Ghez A., Morris M. R., Christou J. C., 2005. ApJ, 624, 742
Telesco C. M., Davidson J. A., Werner M. W., 1996, ApJ, 456, 541
Telesco C. M. et al., 2003, in Iye M., Moorwood A.F., eds, Proc. SPIE Conf. Ser. Vol. 4841, Instrument Design and Performance for Optical/Infrared Ground-based Telescopes. SPIE, Bellingham, p. 913
Viehmann T., Eckart A., Schödel R., Pott J-U., Moultaka J., 2006, ApJ, 642, 861
Zhao J-H., Morris M. R., Goss W. M., An T., 2009, ApJ, 699, 186
Zhao J-H., Blundell R., Downes D., Schuster K. F., Marrone D. P., 2010, ApJ, 723, 1097

This paper has been typeset from a TEX/LATEX file prepared by the author.